



Numerical simulation of lubricated DLC-coated point contacts under infinite sliding conditions

Jonathan Raisin, Nicolas Fillot, Philippe Vergne, David Dureisseix

► To cite this version:

Jonathan Raisin, Nicolas Fillot, Philippe Vergne, David Dureisseix. Numerical simulation of lubricated DLC-coated point contacts under infinite sliding conditions. *Tribology International*, 2019, 133, pp.136-151. 10.1016/j.triboint.2018.12.032 . hal-01997515

HAL Id: hal-01997515

<https://hal.science/hal-01997515v1>

Submitted on 19 Jan 2022

HAL is a multi-disciplinary open access archive for the deposit and dissemination of scientific research documents, whether they are published or not. The documents may come from teaching and research institutions in France or abroad, or from public or private research centers.

L'archive ouverte pluridisciplinaire **HAL**, est destinée au dépôt et à la diffusion de documents scientifiques de niveau recherche, publiés ou non, émanant des établissements d'enseignement et de recherche français ou étrangers, des laboratoires publics ou privés.



Distributed under a Creative Commons Attribution - NonCommercial - NoDerivatives 4.0 International License

Numerical simulation of lubricated DLC-coated point contacts under infinite sliding conditions

DOI: 10.1016/j.triboint.2018.12.032

Jonathan Raisin^{a,1}, Nicolas Fillot^b, Philippe Vergne^b, David Dureisseix^b

^a Centre de Recherche de Solaize (CRoS), Total Marketing Services, Solaize, France

^b Univ Lyon, INSA-Lyon, CNRS, LaMCoS, UMR5259, F-69621, Villeurbanne, France

ABSTRACT

This article examines the influence of low thermal inertia coatings, such as diamond-like carbon coatings, on the lubrication of point contacts operating under zero entrainment velocity conditions. Stationary thermal elasto-hydrodynamic simulations are performed to analyze modifications to the thermal viscosity wedge mechanism induced by the presence of such coatings. Three configurations, namely a steel-steel contact, a DLC coated steel-DLC coated steel contact and a steel-DLC coated steel contact, are investigated. For each configuration, temperature, pressure and film thickness profiles are presented in order to discuss the tribological performances (film thickness and traction) of low inertia coatings under these very specific lubrication conditions. In particular, the detrimental effect of having only one coated surface is highlighted and explained.

1 INTRODUCTION

Since the end of the 20th century and the very important advances in deposition technologies for thin films, amorphous diamond-like carbon (DLC) coatings have received a lot of attention [1]. DLC films have widespread applications as protective coatings in areas such as optical windows, magnetic storage disks, car parts and micro-electromechanical devices. Among other distinctive properties, their ability to mitigate friction and wear, under both dry and lubricated conditions, has made them very desirable for tribological applications [2]. However, despite numerous studies and notable empirical evidence [2-8], the origins of the friction reduction achieved with DLC coatings have remained unclear for years and are still under debate. Different mechanisms have been

¹ Corresponding author jonathan.raisin@total.com

hypothesized in the literature in an attempt to explain the role of DLC coatings in the friction reduction depending on the lubrication conditions. In the boundary lubrication regime, the friction reduction has been linked to the graphitization of a layer of the DLC coating under both the effects of mechanical stresses and temperature [2,8,9]. In the elasto-hydrodynamic lubrication regime, the friction reduction has been originally attributed to boundary slippage at the liquid/DLC interface due to lower surface energy of the coatings [5,7]. However, constraints required for the boundary slippage to occur (surfaces have to be extremely smooth [10,11]), are rarely fulfilled in practical applications. Recently, Björling and his coworkers [6,12,13] proposed another explanation, stating that micrometer thick DLC coatings, act as a thermally insulating barrier, hindering the evacuation of the heat generated in the contact through the solids. Using thermal elasto-hydrodynamic (TEHD) simulations, different authors [14-16] showed that by disrupting the thermal balance, DLC coatings induce higher temperatures in the pressurized region of the contact than for uncoated configurations. These higher temperatures in turn lead to a reduction in viscous friction while barely affecting the film thickness for the range of sliding conditions investigated (up to a slide-to-roll ratio (SRR), i.e. the ratio of the sliding velocity of the contacting surfaces and their mean velocity, of 0.8 in [14]). In addition, Habchi [14] identified the main parameters governing the thermal barrier effect as the thermal inertia of the coating material (defined as $I = \sqrt{\rho_i k_i c_i}$ where ρ_i , k_i and c_i are the density, thermal conductivity and specific heat capacity of the material, respectively) and as the coating thickness, h_{ci} .

In a recent article, the authors presented a numerical analysis on the effects governing the performance of lubricated cam-follower contacts equipping racing car engines [17]. One of the main conclusions drawn from the TEHD simulations concerned the prominent role played by thermal effects during entrainment reversals. Results clearly showed that the retention of a lubricating film able to fully separate the surfaces can be attributed almost solely to the thermal viscosity wedge mechanism [18,19]. For the sake of clarity, the authors did not however consider surface coatings at that stage of the analysis, even though it has become a very common technology in cam-follower systems of automotive engines [20]. The present study therefore aims at investigating the influence of low thermal inertia coatings (such as DLC coatings) on the tribological performance of lubricated contacts. In particular, the study focuses on the zero entrainment velocity (ZEV)/infinite sliding conditions encountered, for instance, in cam-follower systems or cageless ball bearings. In the first stage, stationary TEHD simulations are used to reproduce the lubrication of a steel-steel point contact in ZEV conditions. Reference film thickness and temperature profiles are reported to illustrate the formation of a dimple under the action of the thermal viscosity wedge mechanism.

Then, additional simulations are performed on a DLC coated steel-DLC coated steel point contact to analyze and discuss the influence of the coatings on both film thickness and friction. Finally, the most common configuration in which only one of the contacting surfaces is coated with DLC is considered.

2 MODEL

2.1 Geometry and governing equations

Because this article focuses on understanding the mechanisms behind the lubrication of contacts coated with low thermal inertia materials operating under ZEV conditions rather than on a specific application, a stationary point contact configuration was preferred in this study. In fact, the contact under consideration is typical of ball-on-disc tribometers. As schematized on Fig. 1, it can be reduced to the contact between a (coated) sphere of radius R_2 and a (coated) plane, separated by a thin film of lubricant, and subjected to an external load F .

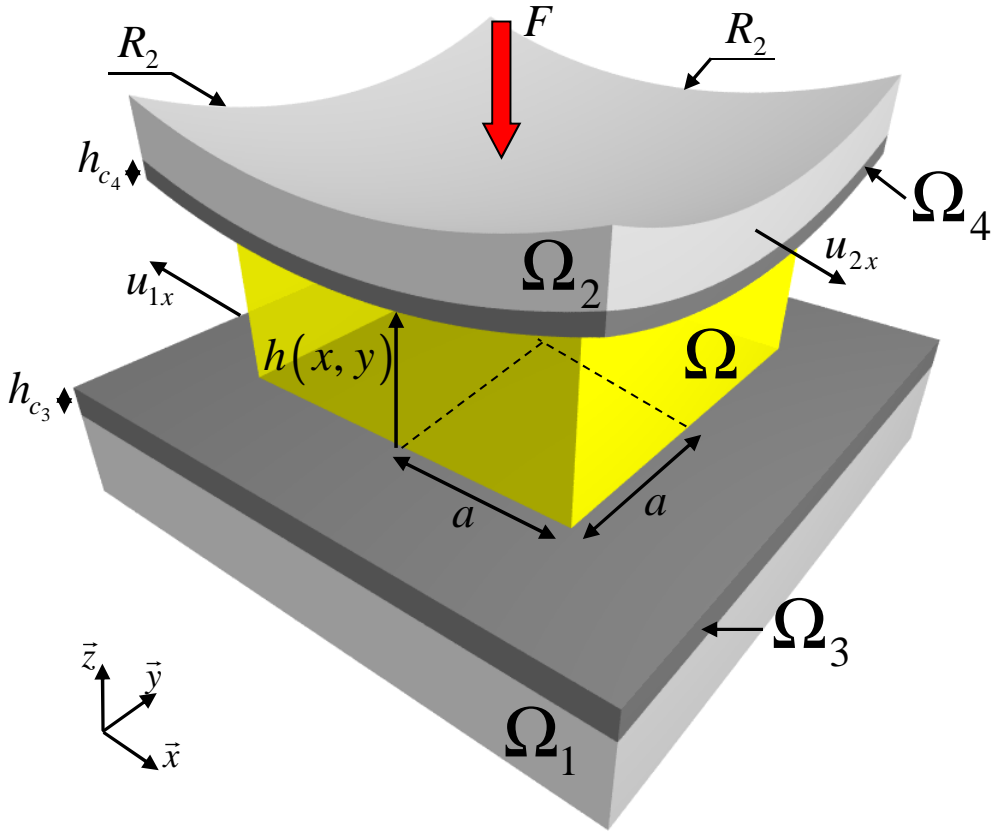


Fig. 1 Typical lubricated point contact between a coated ball and a coated disc. Domain Ω_3 and Ω_4 correspond to the coating of the disc (Ω_1) and ball (Ω_2), respectively. Ω is the fluid domain.

Here, the sphere surface and the plane move only along \vec{x} with respective velocities $u_{2x} > 0$ and $u_{1x} = -u_{2x}$, producing an entrainment velocity, $u_{mx} = \frac{1}{2}(u_{1x} + u_{2x})$ equal to zero (hence the so-called ZEV conditions). Coatings deposited on the disc and the ball have thicknesses h_{c_3} and h_{c_4} , respectively. Finally, surfaces are considered smooth and a fully-flooded lubrication regime is assumed.

From a mathematical point of view, the behavior of these lubricated contacts is modeled using the TEHD formalism described by Habchi [21]. Only the fundamentals of this formalism are recalled hereafter. Readers looking for additional details should refer to the aforementioned reference and Appendix A. The TEHD coupling is achieved through the resolution of four equations, here in their steady-state form. The generalized Reynolds equation [22] describes the fluid flow within the conjunction. The linear elasticity equation computes pressure induced deformations in the solids. Note that, compared to the work of Habchi, the elastic deflection of the coatings was not taken into account in the present study. Indeed, Habchi [23] showed that for thin coatings, such as those considered in this approach, the coatings' contribution to the overall deflection is negligible. In addition, energy equations are solved to obtain the temperature field in the contact (encompassing the fluid, coatings and solids). Finally, the load balance equation completes the coupling by ensuring that the fluid pressure fully balances the applied load.

2.2 Numerical procedure

The numerical model for the simulation of lubricated coated and uncoated point contacts was developed based on the finite element-full system approach proposed by Habchi [21,23], with adaptations by the authors [17,24]. In fact, the present model is a generalization of the line contact version formerly used in [17]. Therefore, the description of the structure and specifics of the model given hereafter will primarily focus on the original feature, i.e. the introduction of the coatings and the subsequent modification in the thermal part of the model.

The TEHL equations, ((A.1) to (A.7) in Appendix A) were first nondimensionalized using the following quantities:

$$\begin{aligned}
\bar{x} = \frac{x}{a}, \bar{y} = \frac{y}{a}, \bar{z} = \begin{cases} z/h, & \text{in the lubricant} \\ z/a & \text{in the solids} \\ z/h_{ci}, i = 3,4 & \text{in the coatings} \end{cases}, \\
\bar{p}(\bar{x}, \bar{y}) = \frac{p(\bar{x}, \bar{y})}{p_h}, H(\bar{x}, \bar{y}) = \frac{h(\bar{x}, \bar{y})R_x}{a^2}, \bar{T}(\bar{x}, \bar{y}, \bar{z}) = \frac{T(\bar{x}, \bar{y}, \bar{z})}{T_0}, \\
\bar{\rho} = \frac{\rho(p, T)}{\rho_0}, \bar{\eta} = \frac{\eta(p, T, \tau)}{\eta_0}.
\end{aligned} \tag{1}$$

where a and p_h are the contact half-width and maximum pressure according to Hertz theory, respectively. ρ_0 and η_0 correspond to the density and viscosity of the lubricant at the ambient temperature T_0 . It can be noted from the new set of dimensionless variables (eq. 1) that the implementation of coatings in the TEHD model adds two other characteristic lengths, i.e. the coatings thicknesses h_{c3} and h_{c4} . In practice, low thermal inertia coatings are usually a few micrometers thick. These new characteristic lengths are thus significantly larger than typical TEHD film thicknesses (ranging from tens to hundreds of nanometers) and yet a few orders of magnitude smaller than typical Hertzian contact half-widths a . Consequently, neither h nor a are suitable to nondimensionalize the simulation domains corresponding to the coatings along \bar{z} . Instead, each coating domain is nondimensionalized using its respective thickness. The resulting dimensionless geometry used for the thermal problem (as well as the one used for the EHD problem) is depicted on Fig. 2.

The dimensionless forms of equation (A.1) through (A.8) (readers interested in these dimensionless forms can refer to [19]) are solved using classical TEHL boundary conditions. The 3D linear elasticity equations are solved on a cube defined for $\bar{x} \in [-30, 30]$, $\bar{y} \in [-30, 30]$ and $\bar{z} \in [-60, 0]$. Null displacements are assumed on the bottom surface while all other surfaces, outside of the contact area, are left free. On the contact surface (materialized by the square shaped domain (Ω) defined for $\bar{x} \in [-4.5, 4.5]$ and $\bar{y} \in [-4.5, 4.5]$), a normal pressure load boundary condition is used to apply the fluid pressure distribution. The latter is obtained from the resolution of the generalized Reynolds equation on Ω with atmospheric pressure as boundary conditions. Cavitation occurring at the exit of the contact is handled by applying the penalty method as in [17,21]. For the thermal part, boundary conditions on the outer surfaces are similar to what was done previously for line contacts [17], i.e. conditional relations are prescribed at the side boundaries of the solid and lubricant domains such that matter entering the contact does so at ambient temperature T_0 . In addition, zero conductive heat fluxes boundary conditions are assumed at the lower and upper solid boundaries (respectively defined by $\bar{z} = -4$ and $\bar{z} = 5$) since they are placed far enough not to be affected by the heat generated in the contact. Finally, the continuity of the

normal heat flux and temperature are imposed at the fluid/coatings interfaces as well as at the coatings/solids interfaces.

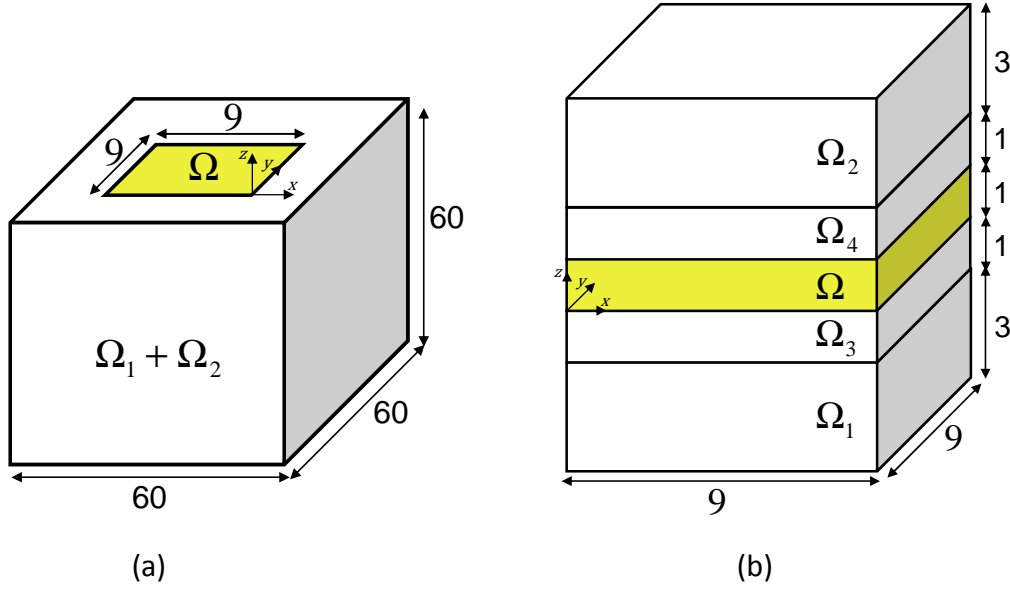


Fig. 2 Geometries of the dimensionless EHD model (a) and of the dimensionless thermal model including coatings (b). For additional details, see [21,23].

The TEHD model for coated point contact was implemented into the commercial finite-element software COMSOL Multiphysics® (COMSOL). The EHD and thermal part (see Fig. 2) were discretized using a combination of structured and unstructured meshes, specifically refined in the pressurized region of the fluid domain. The EHD model contains 35494 tetrahedral elements and 12288 triangular elements (9610 out of the 12288 triangular elements are located inside the circular area delimited by the Hertzian contact half-width, a). The thermal mesh consists of 117613 tetrahedral elements divided as follows: 91909 tetrahedral elements for the fluid film (61889 out of the 91909 are contained in the cylindrical volume delimited by the Hertzian contact half-width), 23065 tetrahedral elements for the coatings and 2639 for the steel substrates. Once fully defined, the lubrication problem is solved in two different stages. Indeed, ZEV conditions generate severe conditions of pressure, shearing and temperature in the contact for which a relevant initial guess can hardly be found. As a consequence, classical solving processes often encounter convergence issues while trying to reach ZEV conditions in a straightforward manner. For instance, using an intermediate isothermal step is not possible as the stationary isothermal ZEV problem has no solution. In order to deal with this issue, specific techniques are required. For instance, Zhang and coworkers used time-dependent solvers along with temporal evolution of the surface velocities to

reach the ZEV conditions in line and point contacts [25,26]. In the present work, a parametric approach was chosen. The final solution, corresponding to the ZEV conditions was obtained as follows: first, the solution for a pure sliding contact ($u_{2x} > 0$ and $u_{1x} = 0$) was computed through the different steps that form the “Initialization stage”. Then, a series of TEHD computations were performed using decreasing values of u_1 until reaching $u_{1x} = -u_{2x}$. For each value of u_{1x} , the fully coupled non-linear system is linearized using a Newton-Raphson procedure and solved using a monolithic approach. Convergence of the solution is considered when the error estimate on each of the dependent variables drops below the relative tolerance of 0.0005. Finally, note that in all the simulations performed, the computational domains of the EHD and thermal problems were reduced by half using the plane of symmetry defined by $y = 0$. Doing so, the TEHD simulations were limited to 602992 degrees of freedom and were solved in about a day on a computer equipped with a Dual Xeon Processor E5-2650 (Intel).

2.3 Materials

Bearing grade steel (100Cr6) was chosen to model the properties of the ball and the disc. As for the coating material, a hydrogenated amorphous **DLC**, a:C-H, containing about 27% of hydrogen was selected (Cavidur from OC Oerlikon). Both the density of the DLC and the coating thickness were provided by the supplier. In the absence of experimental data, thermal conductivity, $k_{3,4}$ and heat capacity, $c_{3,4}$ were estimated using empirical relations in [27] and [28], respectively. All properties related to the solid substrates and coatings are summarized in Table 1 and 2, respectively:

Table 1: Mechanical and thermophysical properties of the 100CR6 solid substrate

| Property | Unit | Value |
|--------------|--|-----------------------|
| $\rho_{1,2}$ | [kg.m ⁻³] | 7850 |
| $E_{1,2}$ | [Pa] | 210 x 10 ⁹ |
| $\nu_{1,2}$ | [-] | 0.3 |
| $c_{1,2}$ | [J.kg ⁻¹ .K ⁻¹] | 470 |
| $k_{1,2}$ | [W.m ⁻¹ .K ⁻¹] | 46 |

Table 2: Mechanical and thermophysical properties of the *DLC* coating

| Property | Unit | Value |
|---------------|--|--------------------|
| $\rho_{3,4}$ | [kg.m ⁻³] | 2000 |
| $c_{3,4}$ | [J.kg ⁻¹ .K ⁻¹] | 885 |
| $k_{3,4}$ | [W.m ⁻¹ .K ⁻¹] | 0.72 |
| $h_{c_{3,4}}$ | [m] | 2×10^{-6} |

The lubricant chosen for the study is a base oil, from group III+ (API classification). Thermophysical properties of the oil were modeled by the authors using extensive characterization data spanning over extensive ranges of temperature and pressure. For more details on the characterization and modeling process, the readers are referred to [29,30]. Lubricant density variations with pressure and temperature are accounted for by the modified Tait equation of state:

$$\rho(p, T) = \rho_r \frac{V_r}{V_0} \times \frac{V_0}{V} \quad (2)$$

$$\text{with } \frac{V_0}{V} = 1 - \frac{1}{1 + K'_0} \ln \left[1 + \frac{p}{K_0} (1 + K'_0) \right]$$

$$\frac{V_r}{V_0} = 1 + a_v(T - T_r)$$

$$K_0 = K_{00} \exp(-\beta_K T)$$

which relates the density at given pressure p and temperature T to the density at a reference state, defined by its temperature T_r and atmospheric pressure p_0 , through volume variations. Parameters required to set the model are: K'_0 , the pressure rate of change of K_0 , the isothermal bulk modulus at p_0 ; a_v the thermal expansivity; β_K is the temperature coefficient of K_0 and K_{00} is the value of K_0 at zero absolute temperature.

As for viscosity, the base oil is assumed to behave as a Newtonian fluid. Only the viscosity variations with pressure and temperature are modeled using the modified WLF-Yasutomi correlation [31]. $\eta(p, T)$ reads:

$$\eta(p, T) = \eta_g \times 10^{\frac{-C_1(T-T_g(p))F_m(p)}{C_2 + (T-T_g(p))F_m(p)}} \quad (3)$$

$$\text{with } T_g(p) = T_g(p_0) + A_1 \ln(1 + A_2 p)$$

$$F_m(p) = (1 + B_1 p)^{B_2}$$

where η_g is the viscosity at the glass transition temperature $T_g(p_0)$. A_1 , A_2 , B_1 , B_2 , C_1 and C_2 are additional fluid-related parameters.

All the properties of the base oil, including the parameters involved in the density and viscosity models, are summarized in Table 3.

Table 3: Parameters and properties defining the lubricant.

| Property | Unit | Value |
|--------------------|--|------------------------|
| Tait EOS | | |
| ρ_r | [kg.m ⁻³] | 825.2 |
| K_0' | [-] | 11 |
| a_v | [K ⁻¹] | 8×10^{-4} |
| T_r | [K] | 288 |
| K_{00} | [Pa] | 9×10^9 |
| β_k | [K ⁻¹] | 6.5×10^{-3} |
| WLF model | | |
| C_1 | [-] | 16.23 |
| C_2 | [K] | 22.54 |
| A_1 | [K] | 94.23 |
| A_2 | [Pa ⁻¹] | 6.37×10^{-10} |
| B_1 | [Pa ⁻¹] | 7.70×10^{-9} |
| B_2 | [-] | -0.48 |
| $T_g(p_0)$ | [K] | 177.95 |
| $\eta(T_g(p_0))$ | [Pa.s] | 10^{12} |
| Thermal properties | | |
| k | [W.m ⁻¹ .K ⁻¹] | 0.16 |
| c | [J.kg ⁻¹ .K ⁻¹] | 2400 |

3 RESULTS AND DISCUSSION

3.1 Steel-steel configuration

In order to establish a reference configuration for the analysis of the influence of low thermal inertia coatings, a first computation was performed for a steel-steel point contact. Velocities of the

sphere surface and the plane were set to $u_{2x} = 2 \text{ m.s}^{-1}$ and $u_{1x} = -2 \text{ m.s}^{-1}$, respectively. A load $F = 2 \text{ N}$ was applied on the sphere of radius $R_2 = 0.0127 \text{ m}$, the corresponding maximum Hertzian pressure is $p_h = 317 \text{ MPa}$. The chosen load may appear small with regards to actual conditions in lubricated applications but, as it will be showed, the intensity of the pressure enhancement due to the thermal viscosity wedge makes convergence quite hard to achieve for the steel-steel configuration. Finally, the ambient temperature was set to $T_0 = 30^\circ\text{C}$ which leads to an ambient viscosity of $\eta_0 = 17.62 \text{ mPa.s}$. Results obtained for the steel-steel configuration are presented in Fig. 3, 4, 5 and B.1.

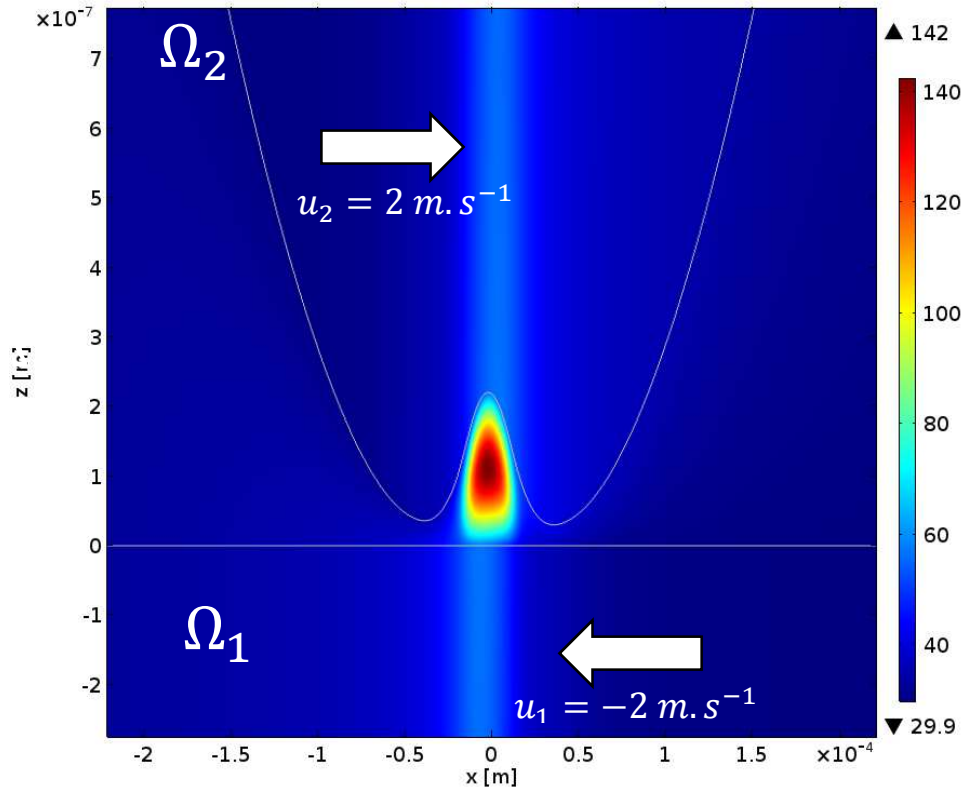


Fig. 3 Temperature (in degrees Celsius) inside the lubricant (Ω) and inside the lower (Ω_1) and upper (Ω_2) solids at the plane of symmetry defined by $y = 0$ for the steel-steel configuration.

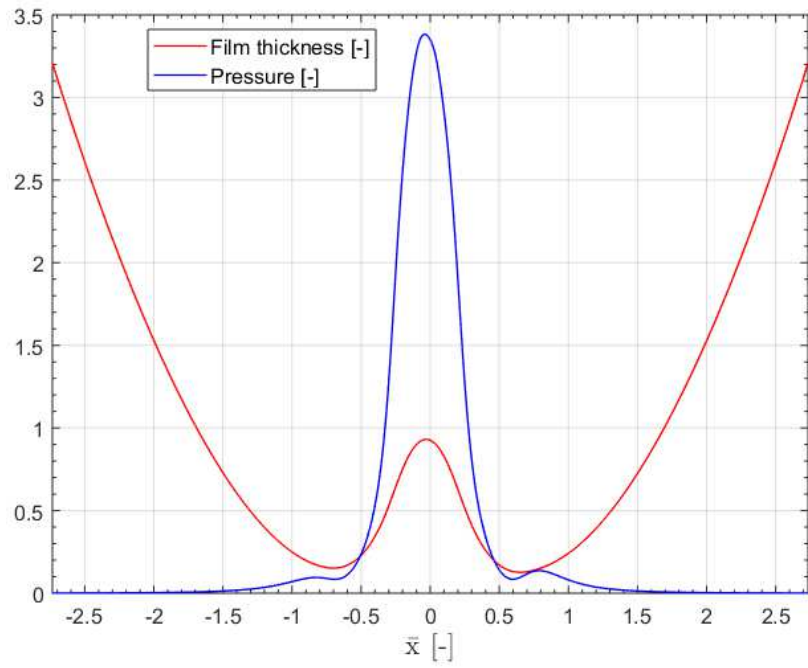
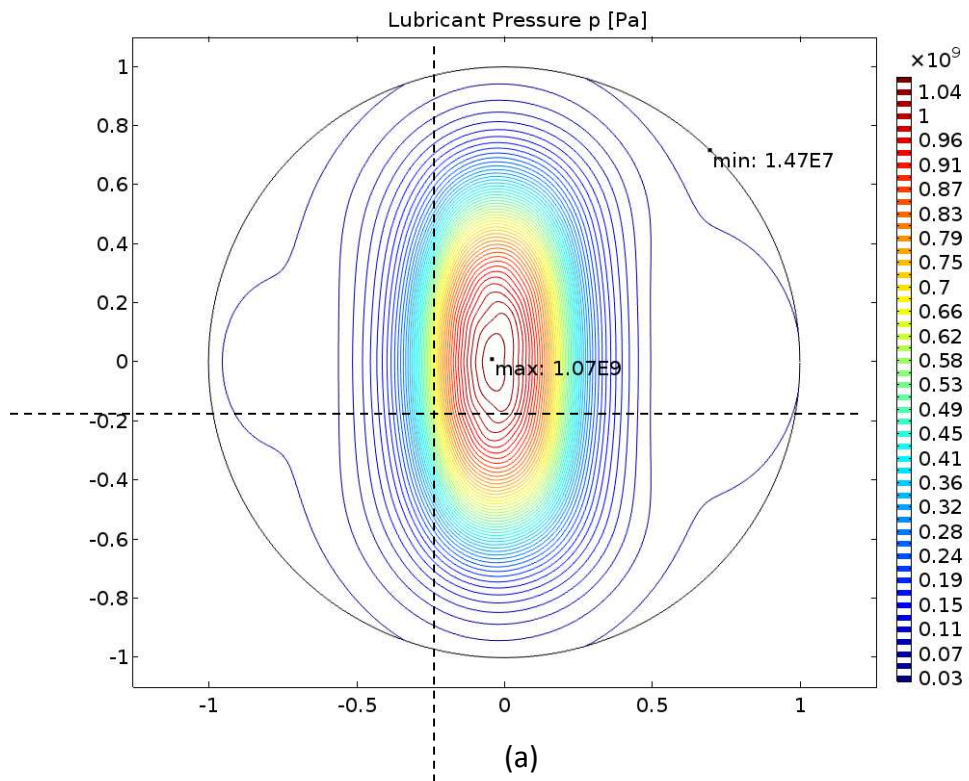


Fig. 4 Dimensionless lubricant pressure and dimensionless film thickness profiles at the plane of symmetry defined by $y = 0$ for the steel-steel configuration.



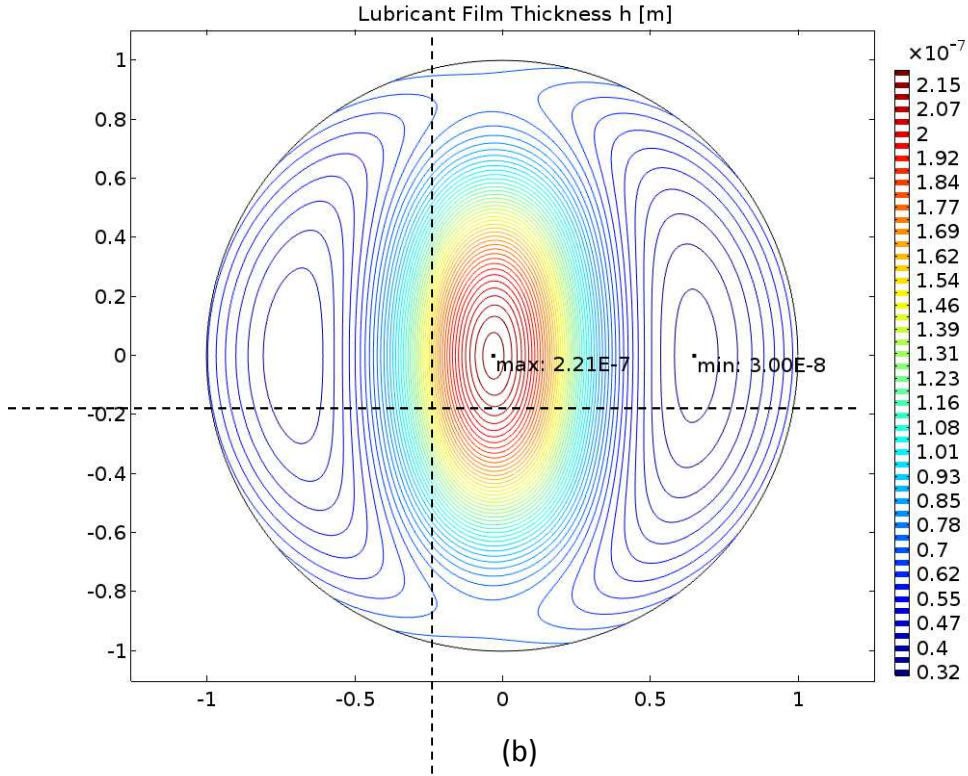


Fig. 5 Lubricant pressure (a) and film thickness (b) maps in the circular area, delimited by the Hertzian contact half-width, for the steel-steel configuration. Note that on Fig. 5, 7 and 11, coordinates are expressed in their dimensionless form.

These three Figures show the remarkable influence of the thermal viscosity wedge mechanism for concentrated steel-steel contacts, even at such a low applied load. In fact, a perfect illustration of this influence is given on Fig. 3 through the temperature increase in the central region of the contact (around $x=0$). Due to the recirculation of a small amount of lubricant trapped in the contact [32], the temperature increases dramatically up to 142°C at a height of half the film thickness, while remaining close to 58°C at the surface of the solids. The intense temperature gradient formed across the film thickness in turn produces strong pressure gradients along the \vec{x} and \vec{y} directions which increase pressure at the center of the contact to about 1.07 GPa (Fig. 5a), i.e. almost 3.5 times the maximum Hertzian pressure (Fig. 4). As a result, the film thickness takes a marked elliptic dimple shape (see Fig. 5) with extrema both located along the plane of symmetry defined by $y=0$ (at least within the circular area delimited by the Hertzian contact half-width, $a = 5.49 \cdot 10^{-4}\text{ m}$). The highest film thickness ($h = 221\text{ nm}$) is reached at the dimple center, which in this case does not exactly correspond to the geometrical contact center (defined by $x = y = 0$). On the opposite, the lowest film thicknesses are located at the boundaries of the dimple (the absolute minimum, $h_m = 30\text{ nm}$, is reached for $\bar{x} > 0$ as seen on Fig. 5b). The location of these minimum

film thicknesses contrasts strongly with those of the common « horse-shoe shaped » film thickness profile encountered in point contacts operating under low to moderate sliding conditions. In fact, in the present case, the two local minimum of film thickness on the contact sides ($\bar{x} = \pm 0.2$ and $\bar{y} = \pm 0.9$ on Fig. 5) remain about two times higher than the absolute minimum reached on the plane of symmetry. This is another consequence of the thermal viscosity wedge effect. Because of the intense pressure gradient reigning between the center of the dimple and the sides, strong Poiseuille flows form along the \vec{y} direction (with velocities up to $u_y = 0.11 \text{ m.s}^{-1}$) allowing significant amounts of lubricant to exit the contact on the sides.

As briefly mentioned above, the temperature, pressure, film thickness and viscosity profiles presented on Figures 3, 4, 5 and B.1 all exhibit a slight asymmetry with respect to the plane defined by $x = 0$. While this observation may appear surprising, readers should bear in mind that the thermal model is not perfectly symmetric in the z direction since, as displayed on Figure 2, we defined $z=0$ on the lower surface and not in the center of the fluid film.

3.2 DLC coated steel-DLC coated steel configuration

When both steel surfaces are coated with a low thermal inertia material (as e.g. the DLC chosen in the present study), the picture is quite different. Because of their very low conductivity (roughly four times the one of the liquid, but only one sixtieth of the one of the solid substrates), the coatings limit the ability of the solids to absorb and evacuate heat produced by the viscous shearing in the lubricant (Fig. 6). Heat therefore remains “trapped” in the contact and significantly affects a large volume of lubricant and the coatings over their entire depth ($h_{c_{3,4}} = 2 \mu\text{m}$). As a consequence, temperatures reached in the lubricant (within the circular area delimited by the Hertzian contact half-width, $a = 5.49 \cdot 10^{-4} \text{ m}$) are, on average, much higher than in the steel-steel configuration (90°C and 47°C respectively). The maximum temperature (around $T = 108^\circ\text{C}$) is however significantly lower in the DLC coated configuration due to the weakening of the thermal viscosity wedge mechanism. This weakening is directly visible on the lubricant film thickness and pressure in the contact. As depicted on Figs. 7, 8 and B.2, the lubricant film exhibits a completely different shape than what was previously observed with the steel- steel configuration (Figs. 3, 4, 5 and B.1).

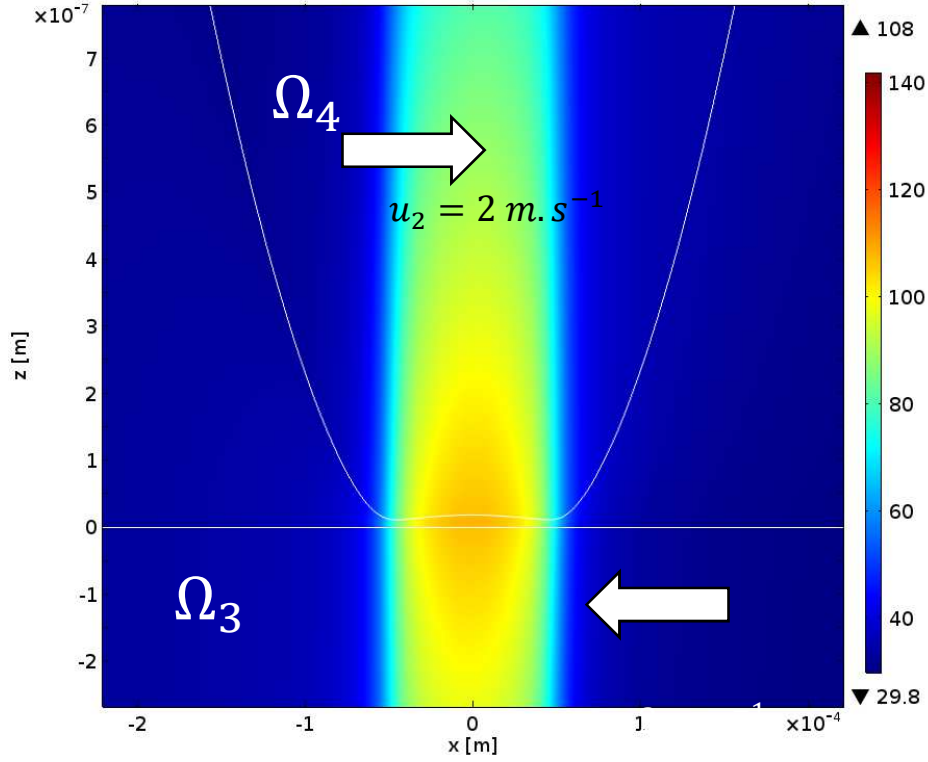


Fig. 6 Temperature (in degrees Celsius) inside the lubricant (Ω) and inside the lower (Ω_3) and upper (Ω_4) coatings at the plane of symmetry defined by $y = 0$ for the DLC coated steel-DLC coated steel configuration. Note that due to the zoom in the z direction, only a small portion of the $2 \mu\text{m}$ thickness of the coatings is visible here.

Firstly, the marked elliptic dimple shape almost disappears in the presence of DLC coatings, becoming significantly much more circular (broader and shallower). The range of film thickness values previously spanning over an order of magnitude is here considerably reduced (down to a factor of about 2.6, see Fig. 7b). Secondly, with the weakening of the thermal viscosity wedge mechanism and its lifting effect, the lubricant film experiences a general decrease in thickness ($h \in [7.3 - 18.8] \text{ nm}$ for the DLC coated configuration compared to $h \in [30 - 221] \text{ nm}$ for the uncoated one). Last but not least, the locations where the clearance is minimal change: they are no longer positioned along the plane of symmetry defined by $y=0$ but rather on the sides of the contact ($\bar{x} = \pm 0.2$ and $\bar{y} = \pm 0.9$ on Fig. 7). Accordingly, side flows are negligible (maximum velocities along the \vec{y} direction within the circular area delimited by the Hertzian contact half-width do not exceed $u_y = 0.01 \text{ m.s}^{-1}$, one tenth of those observed in the uncoated configuration). Most of the lubricant now exits the contact at the boundaries of the dimple ($\bar{x} = \pm 0.85$ on Fig. 7) and close to the plane of symmetry defined by $y=0$. The influence of DLC coatings on the lubricant pressure is also drastic.

With the weakening of the thermal viscosity wedge mechanism, the pressure enhancement vanishes and a pressure profile close to Hertz theory (Fig. 7a and Fig. 8) is recovered.

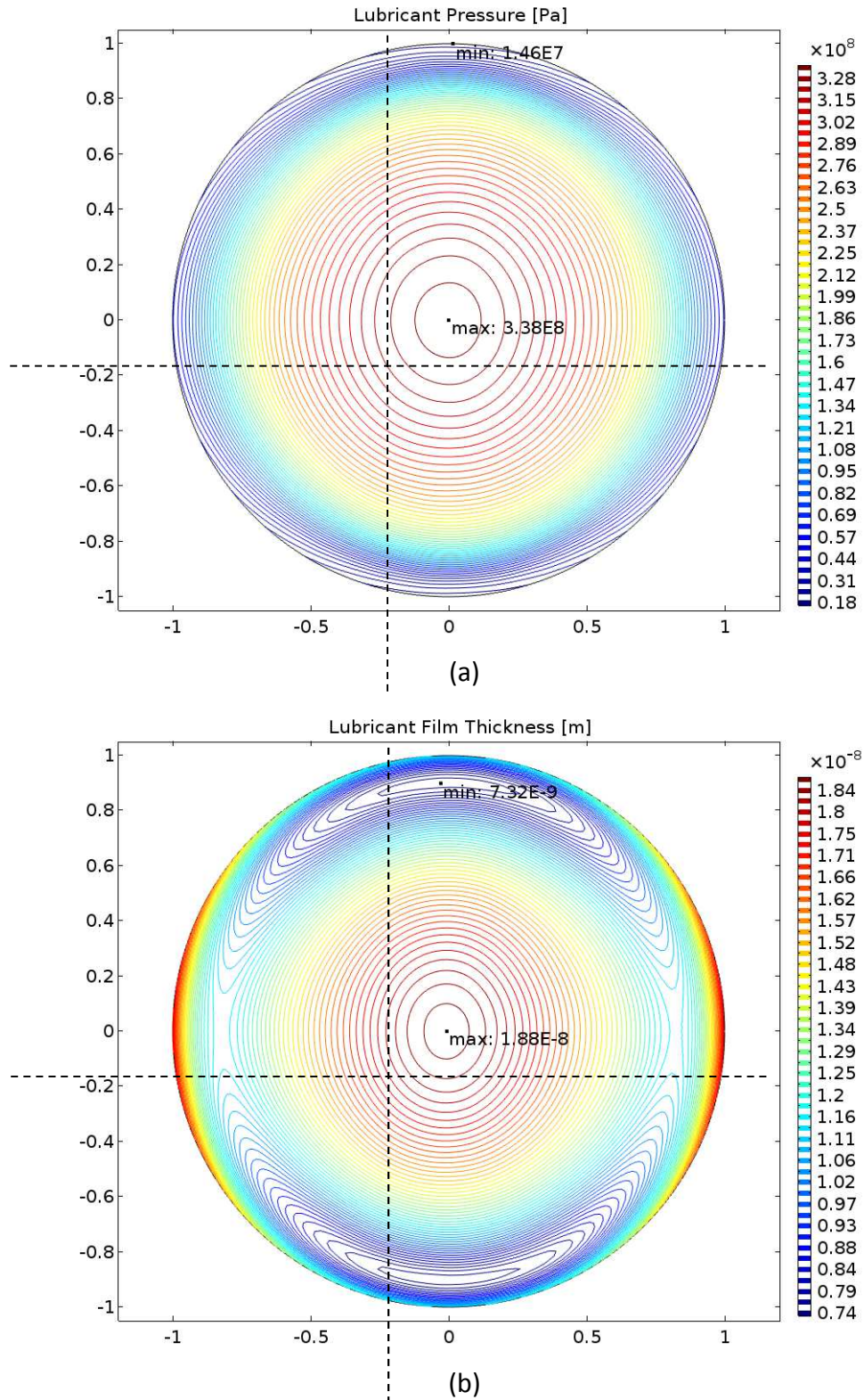


Fig. 7 Lubricant pressure (a) and film thickness (b) maps in the circular area, delimited by the Hertzian contact half-width, of the DLC coated steel-DLC coated steel configuration.

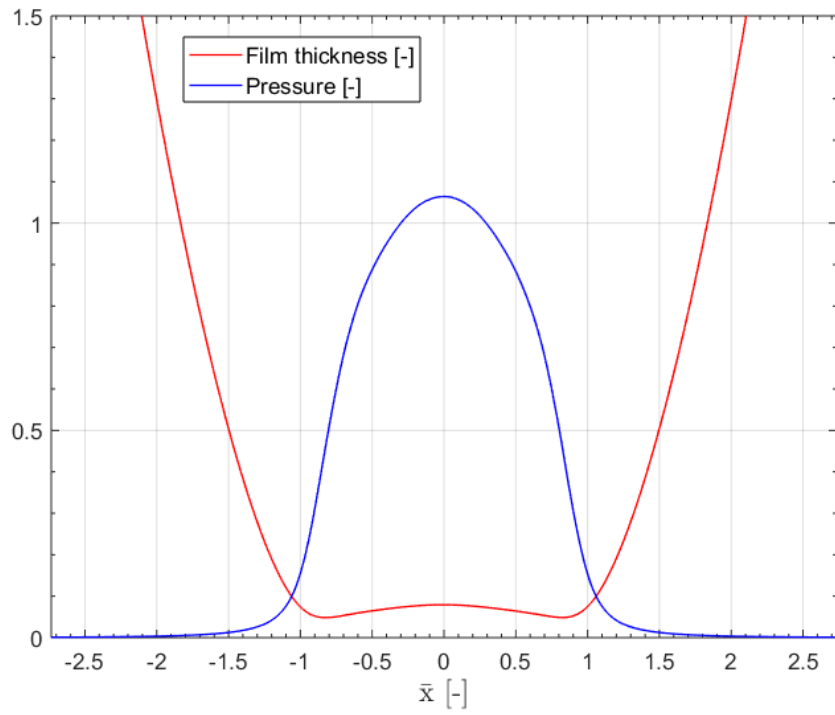


Fig. 8 Dimensionless lubricant pressure and dimensionless film thickness profiles along the entrainment direction (at the plane of symmetry defined by $y = 0$) of the DLC coated steel-DLC coated steel configuration.

3.3 Steel-DLC coated steel configuration

The mixed configuration, i.e. where only one of the solids is coated with a low thermal inertia material, is the most interesting case. Indeed, unlike the two previous configurations, the presence of the DLC coating on the bottom solid only, produces strongly dissymmetrical lubrication conditions (Figs. 9-11). This dissymmetry is illustrated on Fig. 9 in the form of the temperature profile inside the contact along the plane of symmetry defined by $y = 0$. Because of its higher thermal conductivity, heat diffuses much faster in the depth of the upper solid (Ω_2) than in the depth of the lower coating (Ω_3). Hence, temperature along the \vec{z} direction appears constant in Ω_2 while a marked gradient can clearly be distinguished in Ω_3 . In addition, the difference in the thermal properties of the surfaces significantly affect the temperature of the lubricant in the contact. This is especially clear when looking at the viscosity profile inside the lubricant film (Fig. 10). As the upper solid surface (Ω_2) remains (about 6°C) colder than the lower coating surface (Ω_3), viscosity differences appear across the lubricant film.

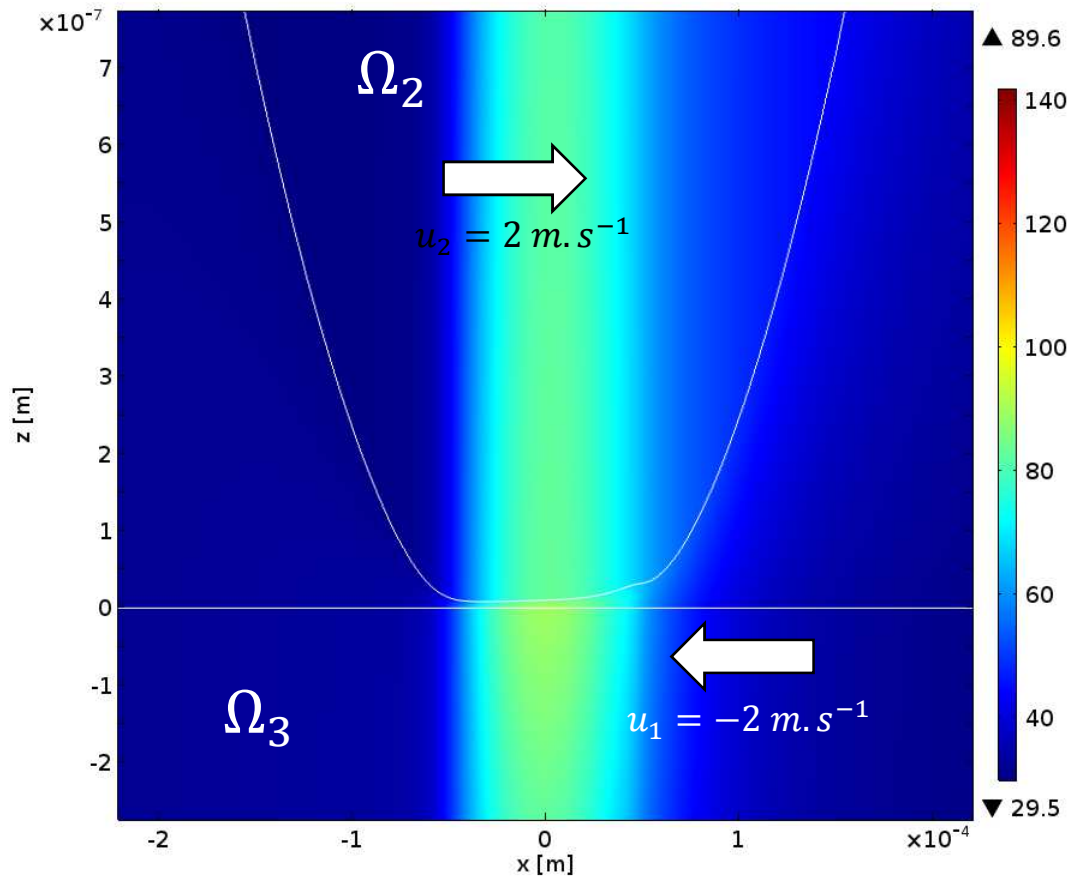


Fig. 9 Temperature (in degrees Celsius) inside the lubricant (Ω) and inside the lower coating (Ω_3) and upper solid (Ω_2) at the plane of symmetry defined by $y = 0$ for the steel-DLC coated steel configuration. Note that due to the zoom in the z direction, only a small portion of the $2\ \mu\text{m}$ thickness of the coating is visible here.

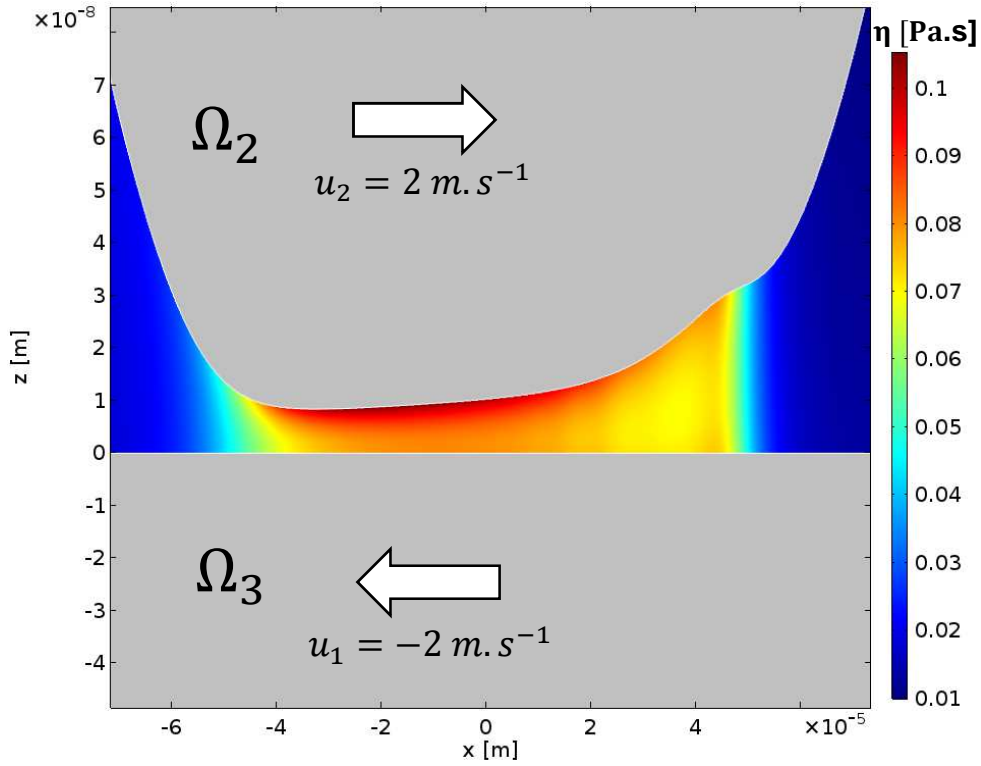


Fig. 10 Lubricant viscosity (in Pa.s) inside the contact at the plane of symmetry defined by $y = 0$ for the steel-DLC coated steel configuration.

The particularity here is that, contrary to the steel-steel configuration, the resulting viscosity gradient across the film has no symmetry. Therefore, the lift effect i.e. the pressure enhancement provided by the thermal viscosity wedge mechanism only appears on a limited portion of the contact, where $x > 0$ (as evidenced by the concentration of isobars at the right side of the contact on Figs 11a). At first, this phenomenon may appear beneficial as it generates film thicknesses larger than those obtained for the DLC coated steel-DLC coated steel configuration in the region where the pressure enhancement is located. However, this localized lifting effect also has a counterpart, i.e. a significant drop of film thickness on the other portions of the contact (Fig.11b). In fact, the drop is so intense that the mixed configuration (i.e. containing a low thermal inertia coating on

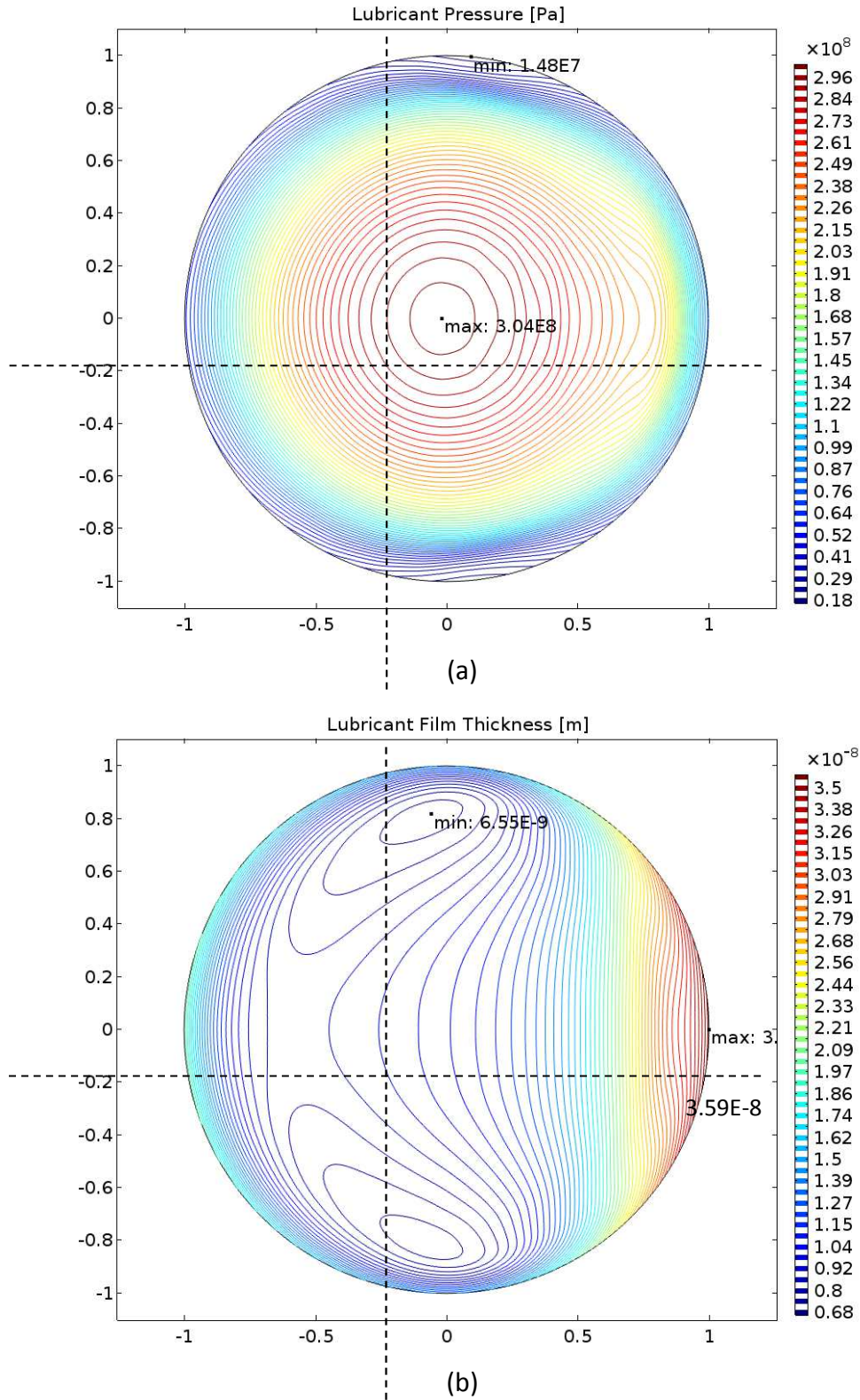


Fig. 11 Lubricant pressure (a) and film thickness (b) maps in the circular area, delimited by the Hertzian contact half-width, of the steel-DLC coated steel configuration.

only one of the solids) produces the smallest film thicknesses making it the least favorable ($h_m = 6.55 \text{ nm}$ compared with 7.32 nm and 30 nm for the DLC coated steel-DLC coated steel and steel-

steel configurations respectively, see Table 4). In order to further analyze the influence of low thermal inertia coatings, the coefficient of traction (or fluid friction) in the x direction, C_f , was also computed for the different configurations as the average of the total shear forces on the upper and lower fluid/solid interfaces divided by the applied force:

$$C_f = \frac{1}{2F} \left(\left| \iint_{\Omega/\Omega_{1-3}} \eta(p, T) \frac{\partial u_x}{\partial z} dx dy \right| + \left| \iint_{\Omega/\Omega_{2-4}} \eta(p, T) \frac{\partial u_x}{\partial z} dx dy \right| \right) \quad (4)$$

where u_x is the fluid velocity along the x direction at any point $M(x, y, z)$ of the fluid film (see Appendix A).

Once again, the mixed configuration performs worse than the other configurations, by a significant margin, with a traction coefficient $C_f = 0.083$ (compared to 0.061 and 0.059 for the DLC coated steel-DLC coated steel and steel-steel configurations respectively). The average film thickness (computed over the circular area delimited by the Hertzian contact half-width) between the mixed and DLC coated configuration being almost identical (12.95 nm compared to 13.01 nm), the difference in terms of traction coefficient is attributed to the lower average temperature in the pressurized region of the contact ($T = 67.8^\circ\text{C}$ for the steel-DLC coated steel configuration compared to 89.9°C for the DLC coated steel-DLC coated steel configuration).

Table 4: Summary of simulation results for the three different configurations.

| | Steel-Steel | DLC-DLC | Steel-DLC |
|-----------------|-------------|---------|-----------|
| P_{max} [GPa] | 1.07 | 0.338 | 0.304 |
| h_c [nm] | 221 | 18.80 | 10.28 |
| h_m [nm] | 30 | 7.32 | 6.55 |
| C_f [-] | 0.059 | 0.061 | 0.083 |

4 CONCLUSIONS

The lubrication of point contacts operating under zero entrainment velocity (ZEV)/infinite sliding conditions was studied using TEHD simulations. More precisely, this article aimed at investigating the influence of low thermal inertia coatings, such as DLC coatings, which are known to affect the heat balance in contacts, in lubrication conditions controlled by the thermal viscosity wedge mechanism. As a first step, the influence of this mechanism was quantified for a steel-steel contact. Thermal elasto-hydrodynamic simulations showed the predominant role played by the

thermal viscosity wedge mechanism. Even at low applied loads, it can enhance the pressure by a tremendous amount (a magnification by a factor of 3.5 was obtained in this study) in the central region of the contact, ultimately resulting in a significant increase of the central and minimum film thickness and the formation of a dimple.

The addition of low thermal inertia coatings on one or both of the steel solids disrupts the thermal balance and the thermal viscosity wedge mechanism. By homogenizing the temperature inside the lubricant, the low thermal inertia coatings strongly hinder the role and intensity of the thermal viscosity wedge mechanism. As a consequence, their presence significantly reduces the central and minimum film thicknesses. However, from a practical point of view, having only one coated surface or both is not equivalent. In the former case, the lubrication conditions become asymmetric following the difference in thermal properties of the surfaces in contact. This mixed configuration produces the lowest minimum film thickness and the highest fluid friction.

In many applications involving lubricated contacts, low thermal inertia coatings have proven their ability to reduce friction, even under full film lubrication. Yet, as shown in this article, the choice to use low thermal inertia coatings (such as **DLC** coatings) for lubricated contact experiencing ZEV/infinite sliding conditions should be made cautiously as they can strongly deteriorate the lubrication conditions, and even cause a transition to mixed/boundary lubrication regimes. For that matter, quantitative elasto-hydrodynamic simulations of the target application including an accurate description of the lubricant and the influence of the microgeometry of the surfaces would provide some important guidance. Finally, if used, low thermal inertia coatings should be applied on both solids in contact.

ACKNOWLEDGMENTS

The authors are deeply grateful to Total Marketing & Services for their financial support. The authors also acknowledge Nicolas Devaux for his significant help in post-treatment rendering.

REFERENCES

- [1] Robertson, J. (2002), "Diamond-like Amorphous Carbon". *Materials Science and Engineering R: Reports*, **37** (4), 129-281.
- [2] Erdemir, A., Bindal, C., Pagan, J., & Wilbur, P. (1995), "Characterization of transfer layers on steel surfaces sliding against diamond-like hydrocarbon films in dry nitrogen". *Surface and Coatings Technology*, **76**, 559-563.
- [3] Voevodin, A. A., Donley, M. S., Zabinski, J. S., & Bultman, J. E. (1995), "Mechanical and tribological properties of diamond-like carbon coatings prepared by pulsed laser deposition". *Surface and Coatings Technology*, **76**, 534-539.
- [4] Habig, K. H. (1995), "Fundamentals of the tribological behaviour of diamond, diamond-like carbon and cubic boron nitride coatings". *Surface and Coatings Technology*, **76**, 540-547.
- [5] Evans, R. D., Cogdell, J. D., Richter, G. A., & Doll, G. L. (2008), "Traction of lubricated rolling contacts between thin-film coatings and steel". *Tribology Transactions*, **52** (1), 106-113.
- [6] Björling, M., Isaksson, P., Marklund, P., & Larsson, R. (2012), "The influence of DLC coating on EHL friction coefficient". *Tribology Letters*, **47** (2), 285-294.
- [7] Kalin, M., & Velkavrh, I. (2013), "Non-conventional inverse-Stribeck-curve behaviour and other characteristics of DLC coatings in all lubrication regimes". *Wear*, **297** (1), 911-918.
- [8] Bouchet, M. I. D. B., Martin, J. M., Avila, J., Kano, M., Yoshida, K., Tsuruda, T., ... & Asensio, M. C. (2017). Diamond-like carbon coating under oleic acid lubrication: Evidence for graphene oxide formation in superlow friction. *Scientific Reports*, **7**, 46394.
- [9] Holmberg, K., Matthews, A., & Ronkainen, H. (1998), "Coatings tribology—contact mechanisms and surface design". *Tribology International*, **31** (1), 107-120.
- [10] Zhu, Y., & Granick, S. (2002), "Limits of the hydrodynamic no-slip boundary condition". *Physical Review Letters*, **88** (10), 106102.
- [11] Choo, J. H., Glovnea, R. P., Forrest, A. K., & Spikes, H. A. (2007), "A low friction bearing based on liquid slip at the wall". *Journal of Tribology*, **129** (3), 611-620.
- [12] Björling, M., Habchi, W., Bair, S., Larsson, R., & Marklund, P. (2014), "Friction reduction in elastohydrodynamic contacts by thin-layer thermal insulation". *Tribology Letters*, **53** (2), 477-486.
- [13] Björling, M., Larsson, R., & Marklund, P. (2014), "The effect of DLC coating thickness on elastohydrodynamic friction". *Tribology Letters*, **55** (2), 353-362.
- [14] Habchi, W. (2016), "Thermal analysis of friction in coated elastohydrodynamic circular contacts". *Tribology International*, **93**, 530-538.

- [15] Beilicke, R., Bobach, L., & Bartel, D. (2016). "Transient thermal elastohydrodynamic simulation of a DLC coated helical gear pair considering limiting shear stress behavior of the lubricant". *Tribology International*, **97**, 136-150.
- [16] Bobzin K, Brögelmann T, Kalscheuer C, et al. A contribution to the thermal effects of DLC coatings on fluid friction in EHL contacts. *Lubrication Science*. 2018; 30:285–299.
- [17] Raisin, J., Fillot, N., Vergne, P., Dureisseix, D., & Lacour, V. (2016), "Transient Thermal Elastohydrodynamic Modeling of Cam–Follower Systems: Understanding Performance". *Tribology Transactions*, **59** (4), 720-732.
- [18] Fogg, A. (1946), "Fluid Film Lubrication of Parallel Thrust Surfaces", *Proceedings of the Institution of Mechanical Engineers*, **155** (1), 49-67.
- [19] Cameron, A. (1958), "The viscosity wedge". *ASLE transactions*, **1** (2), 248-253.
- [20] Yasuda, Y., Kano, M., Mabuchi, Y., & Abou, S. (2003), *Research on diamond-like carbon coatings for low-friction valve lifters* (No. 2003-01-1101). SAE Technical Paper.
- [21] Habchi, W. (2018). *Finite Element Modeling of Elastohydrodynamic Lubrication Problems*. John Wiley & Sons.
- [22] Bou-Saïd, B., Berthe, D., & Najji, B. (1989), "New formulation for lubrication with non-newtonian fluids". *Journal of Tribology*, **111** (1), 29.
- [23] Habchi, W. (2014), "A numerical model for the solution of thermal elasto-hydrodynamic lubrication in coated circular contacts", *Tribology International*, **73**, 57-68.
- [24] Raisin, J., Fillot, N., Dureisseix, D., Vergne, P. and Lacour, V. (2015), "Characteristic times in transient thermal elastohydrodynamic line contacts", *Tribology International*, **82** (Part B), 472-483.
- [25] Zhang, B., Wang, J., Omasta, M., & Kaneta, M. (2015), "Effect of fluid rheology on the thermal EHL under ZEV in line contact". *Tribology International*, **87**, 40-49.
- [26] Zhang, B., Wang, J., Omasta, M., & Kaneta, M. (2016), "Variation of surface dimple in point contact thermal EHL under ZEV condition". *Tribology International*, **94**, 383-394.
- [27] Shamsa, M., Liu, W. L., Balandin, A. A., Casiraghi, C., Milne, W. I., & Ferrari, A. C. (2006), "Thermal conductivity of diamond-like carbon films". *Applied Physics Letters*, **89** (16), 161921.
- [28] Hakovirta, M., Vuorinen, J. E., He, X. M., Nastasi, M., & Schwarz, R. B. (2000), "Heat capacity of hydrogenated diamond-like carbon films". *Applied Physics Letters*, **77** (15), 2340-2342.
- [29] Mary, C., Philippon, D., Lafarge, L., Laurent, D., Rondelez, F., Bair, S. and Vergne, P. (2013), "New Insight into the Relationship Between Molecular Effects and the Rheological Behavior of Polymer-Thickened Lubricants Under High Pressure", *Tribology Letters*, **52** (3), 357-369.

- [30] Mary, C., Philippon, D., Devaux, N., Fillot, N., Laurent, D., Bair, S., & Vergne, P. (2016), "Bridging high pressure rheology and film-forming capacity of polymer-base oil solutions in EHL". *Tribology International*, **93**, 502-510.
- [31] Bair, S., Mary, C., Bouscharain, N. and Vergne, P. (2013), "An improved Yasutomi correlation for viscosity at high pressure", *Proceedings of the Institution of Mechanical Engineers Part J: Journal of Engineering Tribology*, **227** (9), 1056–1060.
- [32] Bruyere, V., Fillot, N., Morales-Espejel, G. E. and Vergne, P. (2012), "Computational fluid dynamics and full elasticity model for sliding line thermal elastohydrodynamic contacts", *Tribology International*, **46**, 3-13.

NOMENCLATURE

| | |
|--------------------------------|---|
| a | Hertzian contact half-width (m) |
| α_v | Thermal expansivity defined for volume linear with temperature (K^{-1}). Used in the Tait equation of state |
| $A_1, A_2, B_1, B_2, C_1, C_2$ | Parameters of the WLF model |
| c | Specific heat capacity of the lubricant ($J.kg^{-1}.K^{-1}$) |
| C_f | Traction (or fluid friction) coefficient (-) |
| c_i | Specific heat capacity of domain Ω_i ($J.kg^{-1}.K^{-1}$) |
| E_i | Young's modulus (Pa). Only for the solids |
| F | External load applied to the contact (N) |
| h | Lubricant film thickness (m) |
| h_{c_i} | Thickness of the coating corresponding to domain Ω_i (m) |
| h_m | Minimum lubricant film thickness (m) |
| h_0 | Spacing between the undeformed solids (m) |
| I | Thermal inertia of a material ($J.m^{-2}.K^{-1}.s^{-1/2}$) |
| k | Thermal conductivity of the lubricant ($W.m^{-1}.K^{-1}$) |
| k_i | Thermal conductivity of domain Ω_i ($W.m^{-1}.K^{-1}$) |
| K_0 | Bulk modulus of the lubricant at atmospheric pressure p_0 and temperature T (Pa). Used in the Tait equation of state |
| K'_0 | Dimensionless pressure rate of change of K_0 (-). Used in the Tait equation of state. |
| K_{00} | Bulk modulus of the lubricant at atmospheric pressure p_0 and zero absolute temperature (Pa). Used in the Tait equation of state. |

| | |
|------------|---|
| p | Pressure (Pa) |
| p_h | Maximum Hertzian pressure (Pa) |
| p_0 | Atmospheric pressure (Pa) |
| SRR | Slide-to-Roll Ratio in the x direction (-). $SRR = \frac{2(u_{2x}-u_{1x})}{u_{1x}+u_{2x}}$. |
| R_x | Equivalent radius of curvature of the solid surfaces along the \vec{x} direction (m). $R_x = (1/R_1 + 1/R_2)^{-1}$. |
| R_y | Equivalent radius of curvature of the solid surfaces along the \vec{y} direction (m). $R_y = (1/R_1 + 1/R_2)^{-1}$. |
| R_1 | Radii of curvature of the plane (m). $R_1 \approx \infty$ |
| R_2 | Radii of curvature of the ball (m). |
| T | Temperature (K) |
| $T_g(p_0)$ | Glass transition temperature of the lubricant at atmospheric pressure (K) |
| T_r | Reference temperature (K) |
| T_0 | Inlet/ambient temperature (K) |
| u_x | Velocity of the lubricant along the \vec{x} direction (m.s ⁻¹) |
| u_y | Velocity of the lubricant along the \vec{y} direction (m.s ⁻¹) |
| u_{ix} | Linear velocity of domain Ω_i along the \vec{x} direction (m.s ⁻¹) |
| u_{iy} | Linear velocity of domain Ω_i along the \vec{y} direction (m.s ⁻¹) |
| u_{mx} | Entrainment velocity along the \vec{x} direction (m.s ⁻¹) |
| V | Total volume occupied by the lubricant at pressure p and temperature T (m ³). Used in the Tait equation of state. |
| V_r | Total volume occupied by the lubricant at atmospheric pressure p_0 and reference temperature T_r (m ³). Used in the Tait equation of state. |

| | |
|------------|--|
| V_0 | Total volume occupied by the lubricant at atmospheric pressure p_0 and temperature T (m^3). Used in the Tait equation of state. |
| w | Total elastic deflection of the solids (m) |
| x | Coordinate in the entrainment direction (m) |
| y | Coordinate in the transverse direction (m) |
| z | Coordinate in the vertical direction (m) |
| β_K | Temperature coefficient of K_0 (K^{-1}). Used in the Tait equation of state. |
| η | Lubricant viscosity at pressure p and temperature T (Pa.s) |
| η_g | Viscosity of the lubricant at the glass transition temperature T_g and atmospheric pressure p_0 (Pa.s) |
| η_0 | Viscosity of the lubricant at atmospheric pressure p_0 and inlet/ambient temperature T_0 (Pa.s) |
| ν_i | Poisson's ratio of domain Ω_i (-). Only for the solids |
| Ω | Fluid/lubricant domain |
| Ω_i | Solid and coatings domains |
| ρ | Density of the lubricant at pressure p and temperature T (kg.m^{-3}) |
| ρ_i | Density of domain Ω_i (kg.m^{-3}) |
| ρ_r | Density of the lubricant at atmospheric pressure p_0 and temperature T_r (kg.m^{-3}) |
| ρ_0 | Density of the lubricant at atmospheric pressure p_0 and inlet/ambient temperature T_0 (kg.m^{-3}) |

APPENDIX A: Equations of the TEHD lubricated point contact problem

As mentioned in section 2.1, the thermal elasto-hydrodynamic formalism was used to simulate the behavior of lubricated point contacts with and without coated surfaces. This formalism consists in the resolution of four classical equations which are detailed hereafter.

The generalized Reynolds equation gives the pressure $p(x, y)$ at any given point inside the fluid domain Ω . Applied to point contacts, the equation reads:

$$-\frac{\partial}{\partial x} \left[\left(\frac{\rho}{\eta} \right)_e \frac{\partial p(x, y)}{\partial x} \right] - \frac{\partial}{\partial y} \left[\left(\frac{\rho}{\eta} \right)_e \frac{\partial p(x, y)}{\partial y} \right] + \frac{\partial}{\partial x} (\rho_x^*) + \frac{\partial}{\partial y} (\rho_y^*) = 0 \quad (\text{A.1})$$

Through the use of integral terms, the generalized Reynolds equation takes into account the influence of cross-film temperature (and possibly shear stress) gradients on the main lubricant properties, density $\rho(p, T)$ and viscosity $\eta(p, T)$. These integral terms are written as:

$$\begin{aligned} \left(\frac{\rho}{\eta} \right)_e &= \frac{\eta_e}{\eta'_e} \rho'_e - \rho''_e \\ \rho_x^* &= \rho'_e \eta_e (u_{2x} - u_{1x}) - \rho_e u_{1x} \\ \rho_y^* &= \rho'_e \eta_e (u_{2y} - u_{1y}) - \rho_e u_{1y} \\ \rho_e &= \int_0^{h(x,y)} \rho(p, T) dz \\ \rho'_e &= \int_0^{h(x,y)} \rho(p, T) \left(\int_0^z \frac{1}{\eta(p, T)} dz' \right) dz \\ \rho''_e &= \int_0^{h(x,y)} \rho(p, T) \left(\int_0^z \frac{z'}{\eta(p, T)} dz' \right) dz \\ \frac{1}{\eta_e} &= \int_0^{h(x,y)} \frac{1}{\eta(p, T)} dz \\ \frac{1}{\eta'_e} &= \int_0^{h(x,y)} \frac{z}{\eta(p, T)} dz \end{aligned} \quad (\text{A.2})$$

with $h(x, y)$ the film thickness. It is expressed as:

$$h(x, y) = h_0 + \frac{1}{2} \left(\frac{x^2}{R_x} + \frac{y^2}{R_y} \right) - w(x, y) \quad (\text{A.3})$$

and results from the superposition of the rigid body displacement h_0 , the initial undeformed geometry, represented by the equivalent radii of curvature of the solid surfaces along the \vec{x} and \vec{y} directions, R_x and R_y and $w(x, y)$, the combined elastic deflection of both solids. This deflection is deduced from the calculation of the displacement vector \mathbf{U} on an equivalent body (see Fig. 2), the mechanical properties of which (Young's modulus and Poisson's ratio), are a combination of those of the two solids [21]. The displacement vector directly stems from the solution of the linear elasticity equation:

$$-\nabla \cdot \sigma = 0 \quad (\text{A.4})$$

with $\sigma = C: \epsilon_s(\mathbf{U})$ where C is the fourth-order stiffness tensor and ϵ_s is the infinitesimal strain tensor.

The load balance equation completing the EHD coupling reads:

$$\int_{\Omega} p(x, y) dx dy = F \quad (\text{A.5})$$

with F , the applied external load.

Finally, the energy-balance equations model the heat generation and transfer in the solids, in the coatings and in the lubricant. Within the solids, heat advection in the \vec{z} direction is neglected following the thin-film assumption (zero velocity in the z direction). Neglecting body forces and heat radiation, the energy-balance equations for the solids Ω_1 and Ω_2 and for the coatings Ω_3 and Ω_4 reduces to:

$$\rho_i c_i \left(u_{ix} \frac{\partial T}{\partial x} + u_{iy} \frac{\partial T}{\partial y} \right) - \frac{\partial}{\partial x} \left(k_i \frac{\partial T}{\partial x} \right) - \frac{\partial}{\partial y} \left(k_i \frac{\partial T}{\partial y} \right) - \frac{\partial}{\partial z} \left(k_i \frac{\partial T}{\partial z} \right) = 0 \quad (\text{A.6})$$

$i = 1, 2, 3, 4$

where ρ_i , c_i and k_i are the thermophysical properties (density, heat capacity and thermal conductivity) of the material corresponding to domain Ω_i , respectively. Within the fluid Ω , advection in both the \vec{x} and \vec{y} directions dominates over diffusion along the entrainment direction. This allows to further simplify the energy-balance equation:

$$\begin{aligned}
& \rho c \left(u_x(x, y, z) \frac{\partial T}{\partial x} + u_y(x, y, z) \frac{\partial T}{\partial y} \right) - \frac{\partial}{\partial z} \left(k \frac{\partial T}{\partial z} \right) \\
&= - \frac{T}{\rho} \frac{\partial \rho(p, T)}{\partial T} \left(u_x(x, y, z) \frac{\partial p}{\partial x} + u_y(x, y, z) \frac{\partial p}{\partial y} \right) \\
&+ \eta \left(\left(\frac{\partial u_x(x, y, z)}{\partial z} \right)^2 + \left(\frac{\partial u_y(x, y, z)}{\partial z} \right)^2 \right)
\end{aligned} \tag{A.7}$$

where $u_x(x, y, z)$ and $u_y(x, y, z)$ are the fluid velocity along \vec{x} and \vec{y} , respectively. These are expressed as:

$$\begin{aligned}
u_x(x, y, z) &= \frac{\partial p}{\partial x} \left(\int_0^z \frac{z'}{\eta} dz' - \frac{\eta_e}{\eta'_e} \int_0^z \frac{1}{\eta} dz' \right) + \eta_e (u_{2x} - u_{1x}) \int_0^z \frac{1}{\eta} dz' + u_{1x} \\
u_y(x, y, z) &= \frac{\partial p}{\partial y} \left(\int_0^z \frac{z'}{\eta} dz' - \frac{\eta_e}{\eta'_e} \int_0^z \frac{1}{\eta} dz' \right) + \eta_e (u_{2y} - u_{1y}) \int_0^z \frac{1}{\eta} dz' + u_{1y}
\end{aligned} \tag{A.8}$$

The first and second right-hand side terms in eq. (A.7) account for the production of heat by compression and shearing, respectively.

APPENDIX B: Viscosity profile in the steel-steel and DLC coated steel-DLC coated steel configurations

In order to better understand the effect and intensity of the thermal viscosity wedge, the viscosity profiles obtained in the simulations for the steel-steel and DLC coated steel-DLC coated steel configurations are presented on Figs. B.1 and B.2 respectively. Note that, because the viscosity values are strongly different from a quantitative point of view, each figure has a specific color scale.

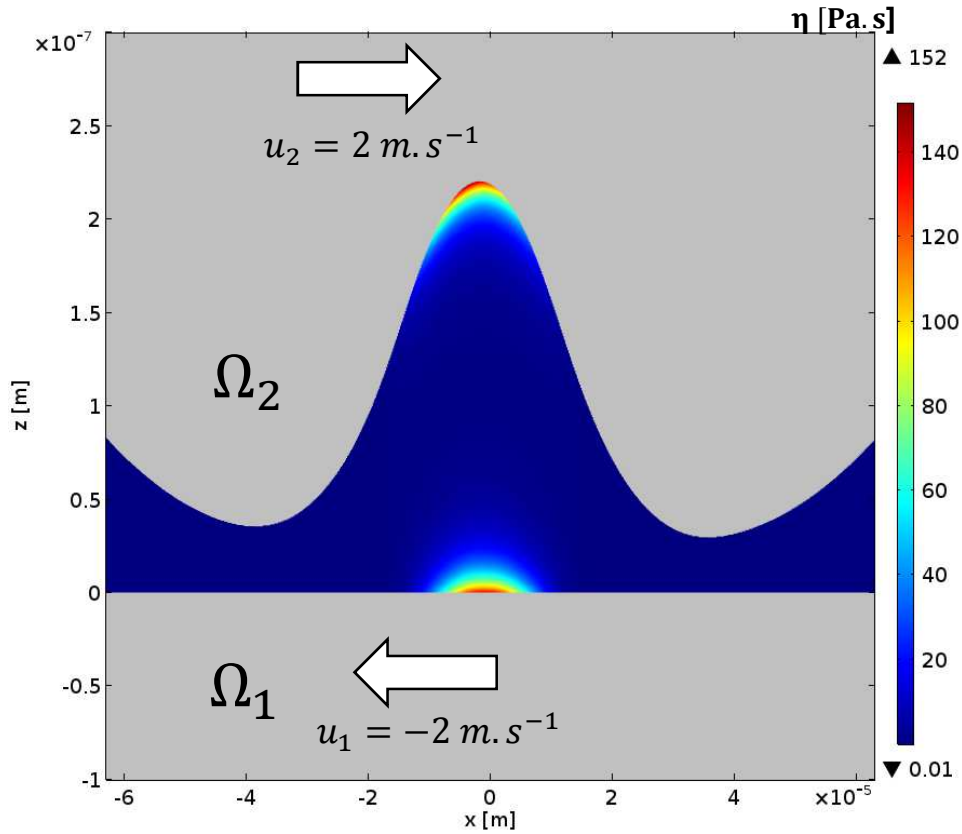


Fig. B.1 Viscosity (in Pa.s) of the lubricant (Ω) inside the contact at the plane of symmetry defined by $y = 0$ for the steel- steel configuration.

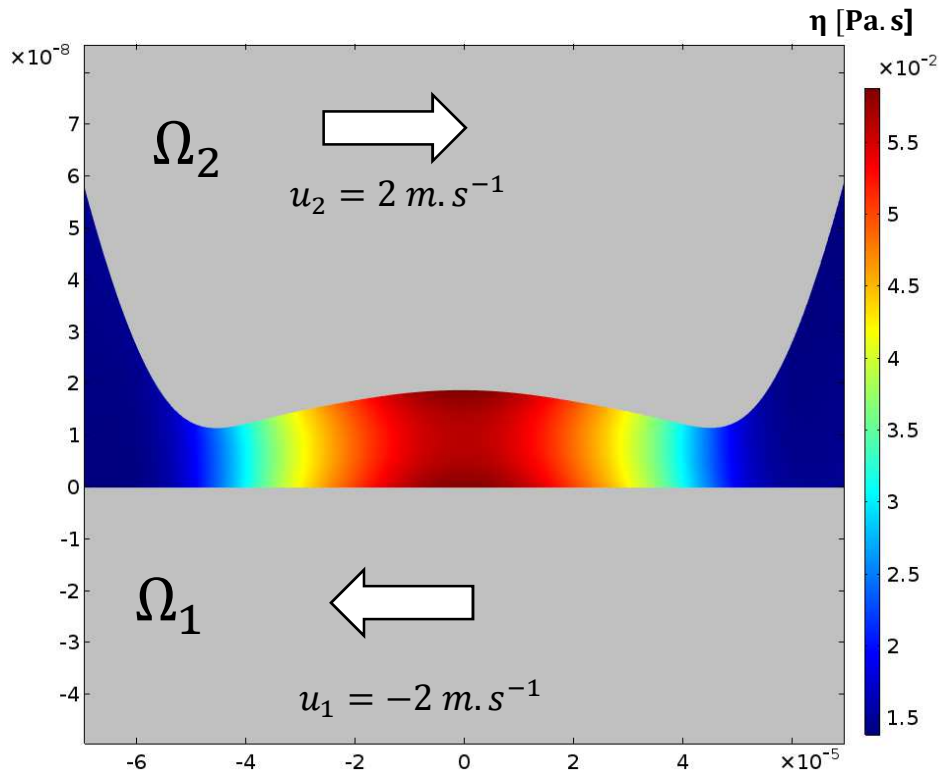


Fig. B.2 Viscosity (in Pa.s) of the lubricant (Ω) inside the contact at the plane of symmetry defined by $y = 0$ for the DLC coated steel-DLC coated steel configuration.